

Coherent Elastic Neutrino-Nucleus Scattering with directional detectors

M. Abdullah,^{1,*} D. Aristizabal Sierra,^{2,3,†} Bhaskar Dutta,^{1,‡} and Louis E. Strigari^{1,§}

¹*Department of Physics and Astronomy, Mitchell Institute for Fundamental Physics and Astronomy, Texas A&M University, College Station, TX 77843, USA*

²*Universidad Técnica Federico Santa María - Departamento de Física, Casilla 110-V, Avda. España 1680, Valparaíso, Chile*

³*IFPA, Dep. AGO, Université de Liège, Bat B5, Sart Tilman B-4000 Liège 1, Belgium*

We study the sensitivity of detectors with directional sensitivity to coherent elastic neutrino-nucleus scattering (CEvNS), and how these detectors complement measurements of the nuclear recoil energy. We consider stopped pion and reactor neutrino sources, and use gaseous helium and fluorine as examples of detector material. We generate Standard Model predictions, and compare to scenarios that include new, light vector or scalar mediators. We show that directional detectors can provide valuable additional information in discerning new physics, and we identify prominent spectral features in both the angular and the recoil energy spectrum for light mediators, even for nuclear recoil energy thresholds as high as ~ 50 keV. Combined with energy and timing information, directional information can play an important role in extracting new physics from CEvNS experiments.

I. INTRODUCTION

Coherent Elastic Neutrino-Nucleus Scattering (CEvNS) has proven to be a powerful test of the Standard Model (SM) of particle physics, and a search tool for new physics (NP). In particular, the recent detections of CEvNS by COHERENT [1, 2] is able to constrain non-standard neutrino interactions (NSI) due to heavy or light mediators [3–12], generalized scalar and vector neutrino interactions [13], and hidden sector models [14]. It also sets independent constraints on the effective neutron size distribution of CsI [15–17], and on sterile neutrinos [18, 19].

To this point, constraints on NP with the COHERENT data have been obtained mostly using the measured distribution of nuclear recoil energies. Due to the nature of the stopped-pion source utilized by COHERENT and the detectors that are deployed, the time distribution of events also provides a powerful probe of NP models [20, 21]. This has proven to be important not only in searches for NP in the neutrino sector, but also applicable to searches for NP in the form of low-mass dark matter [22].

Since the power of CEvNS as a NP probe is just now beginning to be realized, it is important to identify new ways to exploit CEvNS in future experiments. In this paper, we take a step in this direction and investigate the prospects for supplementing the nuclear recoil energy with the direction of the nuclear recoil. Assuming SM physics, we calculate the expected angular distribution of nuclear recoil events for terrestrial sources that are now being used for the detection of CEvNS. We extend to investigate the angular dependence of

CEvNS in NP scenarios, in particular focusing on models with MeV-scale vector or scalar mediators.

While directional detectors are not currently being deployed for detecting CEvNS from terrestrial sources, research and development for similar detectors is being actively pursued for the purpose of dark matter detection [23, 24]. Since our analysis is primarily focused on the theoretical aspects of the energy and directional dependence of the induced nuclear recoils, we focus on simplified detectors models. For neutrino sources, we consider both a stopped-pion source and a reactor source. The results that we present are meant to guide both the theoretical and experimental efforts on this topic.

The remainder of this paper is organized as follows. In Section II, we review the theoretical aspect of CEvNS, laying out the formalism for the calculation of the angular distribution of recoil events. In Section III, we discuss the properties of the sources that we consider, and the simple models for the detectors. In Section IV, we review some aspects of the kinematics that are important for our analysis. In Section V we make predictions for SM signatures, and in Section VI we make predictions for NP vector and scalar mediator models.

II. THE RECOIL ENERGY AND DIRECTIONAL RECOIL SPECTRUM

CEvNS is a two-to-two process and therefore the scattering cross section depends only on a single degree of freedom. This is often chosen as the recoil energy, a convenient choice for most experimental designs. The differential event rate as a function of the recoil energy dR/dE_r , or the recoil spectrum (RS) for short, can be expressed as follows:

$$\frac{dR}{dE_r} = \mathcal{N} \int_{E_\nu^{\min}}^{E_\nu^{\max}} \frac{d\sigma}{dE_r} F^2(E_r) \frac{d\Phi}{dE_\nu} dE_\nu, \quad (1)$$

where \mathcal{N} is the number of scattering targets, $d\sigma/dE_r$ is the differential cross section as a function of the recoil energy, E_ν

* mabdullah@tamu.edu

† daristizabal@ulg.ac.be

‡ dutta@physics.tamu.edu

§ strigari@tamu.edu

is the incident neutrino energy, $d\Phi/dE_\nu$ is the neutrino flux, and $F(E_r)$ is the nuclear form factor. We use the Helm form factor [25] given by¹

$$F(E_r) = F_H(q) = 3 \frac{j_1(q)}{qr_n} e^{-(qs)^2/2}, \quad (2)$$

which assumes that the nucleonic distribution is determined by a convolution of a uniform density of radius r_n and a Gaussian profile parametrized by the folding width s , which ‘‘measures’’ the surface thickness. In (2) the momentum transfer is given by $q = \sqrt{2m_N E_r}$, $j_1(q)$ is the spherical Bessel function of the first kind, $s = 0.9$ fm, and $r_n = \sqrt{5/3(R_{\min}^2 - 3s^2)}$. For the targets that we consider below, we have $R_{\min} = 1.6755$ fm for He and 2.8976 fm for F, which correspond to the rms radii of their proton distributions [26].

The SM differential cross section proceeds through a neutral current process and is given by [27, 28]

$$\frac{d\sigma}{dE_r} = \frac{G_F^2 m_N}{2\pi} g_V^2 \left(2 - \frac{m_N E_r}{E_\nu^2} \right), \quad (3)$$

where G_F is the Fermi constant, $g_V = N(g_V^u + 2g_V^d) + Z(2g_V^u + g_V^d)$, $N = A - Z$ with A the nucleus mass number, Z is the atomic number, m_N is the nuclear mass of the detector material, $g_V^u = 1/2 - 4/3 \sin^2 \theta_W$ and $g_V^d = -1/2 + 2/3 \sin^2 \theta_W$. For the Fermi constant and the weak mixing angles we use their PDG values: $G_F = 1.166 \times 10^{-5} \text{ GeV}^{-2}$, $\sin^2 \theta_W = 0.231$. The latter obtained using the $\overline{\text{MS}}$ renormalization scheme at the m_Z scale [29].

We now proceed to generalize the formalism to detectors with directional sensitivity. Theoretically, the E_r dependence in Eq. (1) can be traded with the direction of recoil $\cos \theta_r$ converting the RS to an Angular Spectrum (AS). In practice, however, a detector may provide a measurement of both E_r and $\cos \theta_r$ at once, so it would be more convenient to express the scattering rate as a function of both variables:

$$\frac{d^2 R}{dE_r d\Omega_r}, \quad (4)$$

where Ω_r refers to the solid angle along the direction of the recoiling nucleus with respect to the incoming neutrino direction. We refer to this observable as the Directional Recoil Spectrum (DRS), although the term ‘‘Momentum Spectrum’’ has been previously used in the literature [30]. To derive an expression for the DRS we closely follow Ref. [31] where the incoming neutrino energy E_ν is traded for the angle of the recoiling nucleus. Note that if the neutrino source is monoenergetic this procedure is superfluous; the two arguments of the resulting DRS would be tied by a Dirac δ -function.

The procedure requires some adaptation for neutrino production at the SNS or nuclear reactors. The direction of the

source has no seasonal dependence as in [31] where the neutrinos produced in the Sun whose location with respect to the Earth changes with time. We are interested in terrestrial neutrino sources that are at rest with respect to the detector and so the neutrino flux can be written as

$$\frac{d^2 \Phi}{dE_\nu d\Omega_\nu} = \frac{d\Phi}{dE_\nu} \delta(\hat{q}_\nu - \hat{q}_{\text{det}}), \quad (5)$$

where the unit vector \hat{q}_{det} points from the source to the detector while \hat{q}_ν defines the direction of the incoming neutrino. Strictly speaking this expression should be thought of as per event since both the source and detector are extended objects.

In deriving the cross section in Eq. (3) a 4-dimensional δ -function is evaluated completely. Here we take a step back and leave the energy component of that δ -function that relates the incoming neutrino energy E_ν with E_r . The result is

$$d^2 \sigma = \frac{1}{64\pi^2} \frac{1}{E_\nu m_N} \frac{p'_N dE'_N d\Omega_r}{E'_V} \delta(E'_V + E'_N - E_\nu - m_N) |\mathcal{M}|^2. \quad (6)$$

Here we have used for the relative velocity $v_{\text{rel}} = 1$ and the primed (unprimed) kinematic variables refer to outgoing (incoming) states. Three-momentum conservation combined with energy conservation $E_r = E'_N - m_N$ allows us to write the argument of the δ -function as a function of $\cos \theta_r$, where the nucleus recoil angle θ_r is measured with respect to the incoming neutrino direction, i.e. $\cos \theta_r = \hat{q}_{\text{det}} \cdot \hat{q}_r$:

$$f(\cos \theta_r) \equiv E_r + \sqrt{E_\nu^2 + p_N'^2 - 2E_\nu p'_N \cos \theta_r} - E_\nu. \quad (7)$$

Using the δ -function identity

$$\delta[f(\cos \theta_r)] = \frac{\delta(\cos \theta_r - \cos \bar{\theta}_r)}{|df(\cos \theta_r)/d \cos \theta_r|}, \quad (8)$$

with $\cos \bar{\theta}_r = (m_N + E_\nu)/E_\nu \sqrt{E_r/(2m_N + E_r)}$, the root of the equation $f(\cos \theta_r) = 0$, we arrive at a rather simplified expression for the double differential cross section [31]

$$\frac{d^2 \sigma}{dE_r d\Omega_r} = \frac{1}{2\pi} \frac{d\sigma}{dE_r} \delta(\cos \theta_r - \cos \bar{\theta}_r). \quad (9)$$

The DRS in (4) can now be written as

$$\frac{d^2 R}{dE_r d\Omega_r} = \mathcal{N} \int \frac{d^2 \sigma}{dE_r d\Omega_r} F^2(E_r) \frac{d^2 \Phi}{dE_\nu d\Omega_\nu} dE_\nu d\Omega_\nu \quad (10)$$

which with the aid of Eqs. (5) and (9) becomes

$$\frac{d^2 R}{dE_r d\Omega_r} = \frac{\mathcal{N}}{2\pi} \int \frac{d\sigma}{dE_r} F^2(E_r) \frac{d\Phi}{dE_\nu} \delta(\hat{q}_r \cdot \hat{q}_{\text{det}} - \cos \bar{\theta}_r) dE_\nu. \quad (11)$$

To perform the integration we rewrite the argument of the δ -function as

$$\hat{q}_r \cdot \hat{q}_{\text{det}} - \cos \bar{\theta}_r = E_\nu^{\min} \left(x + \frac{1}{\varepsilon} \right), \quad (12)$$

with the new variables defined by

$$\frac{1}{\varepsilon} = \frac{\hat{q}_r \cdot \hat{q}_{\text{det}}}{E_\nu^{\min}} - \frac{1}{m_N}, \quad x = -\frac{1}{E_\nu} \quad (13)$$

¹ Any other choice as well as accounting for different proton and neutron distributions through independent proton and neutron form factors will have only a percent level effect, in particular for light nuclei such as those we consider here [16].

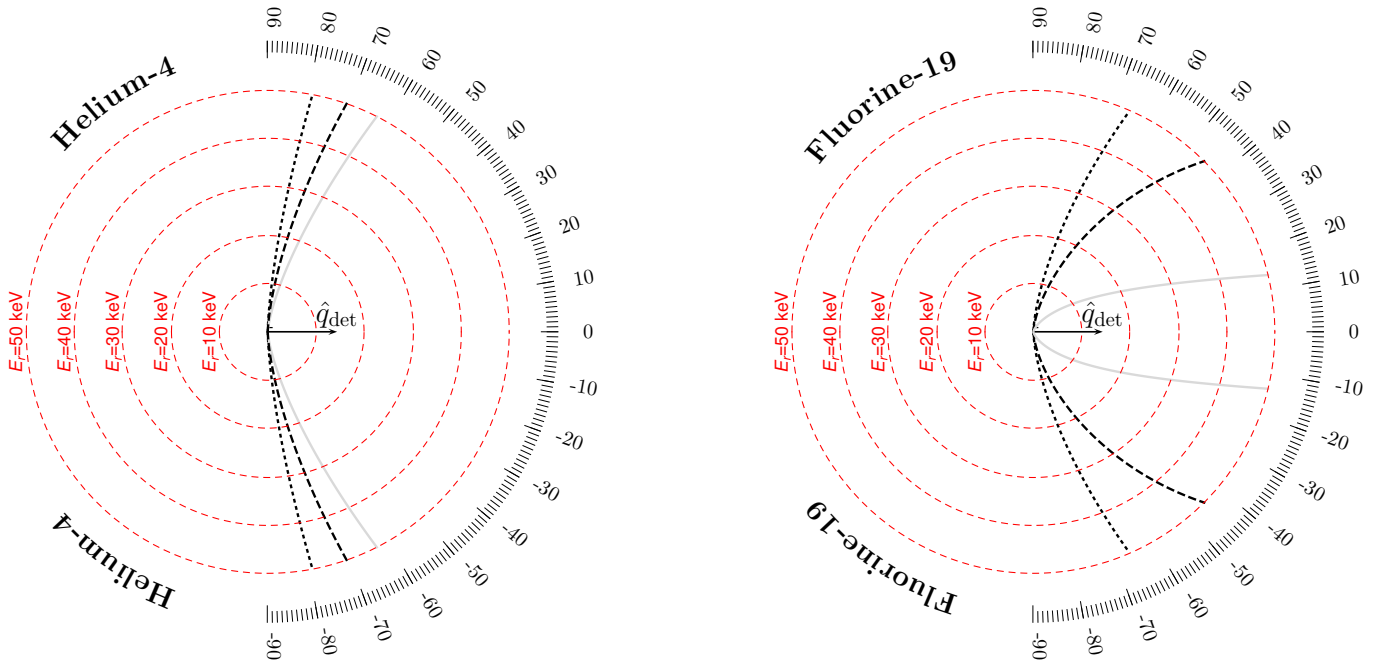


FIG. 1. **Left:** Allowed nuclear recoil angular region for a particular incoming neutrino direction (determined by the unit vector \hat{q}_{det} which points from the neutrino source to the detector) for SNS and a helium detector. We include $\theta_r \rightarrow -\theta_r$ for illustration. The dotted black curve is determined by the kinematic constraint $E_\nu = \varepsilon = m_\mu/2$ enforced by energy conservation and the neutrino production mechanism. The grey solid curve is the single event threshold $d^2R/dE_r d\Omega_r \geq 1$, assuming an exposure of one ton-yr. The dashed black curve is the angular position of the ν_μ events due to the mono-energetic neutrinos (see Eq. (19)). The red dashed lines are contours of equal recoil energy. Given an incoming neutrino direction the measurable angular distribution lies to the right of the dotted black curves. **Right:** Same as the left graph but for a fluorine detector.

and we used $E_\nu^{\min} = \sqrt{m_N E_r/2}$. Integration over x yields the following analytical expression for the DRS

$$\frac{d^2R}{dE_r d\Omega_r} = \frac{\mathcal{N}}{2\pi} \frac{d\sigma}{dE_r} \Big|_{E_\nu=\varepsilon} F^2(E_r) \frac{\varepsilon^2}{E_\nu^{\min}} \frac{d\Phi}{dE_\nu} \Big|_{E_\nu=\varepsilon}. \quad (14)$$

Dependence on the nucleus scattering angle is encoded in ε through $\hat{q}_r \cdot \hat{q}_{\text{det}} = \cos \theta_r$.

III. SOURCE AND DETECTOR MODELING

As emphasized above we are interested in understanding the basic physics of directionality in CEvNS and will, therefore, take a simplified approach in modeling the neutrino sources and detectors.

A. Neutrino sources

For the pion source we will assume the setup similar to that of the COHERENT experiment at the Oak Ridge National Laboratory. The neutrinos are produced at the Spallation Neutrino Source (SNS) by stopped pion decays (prompt ν_μ) and consequent μ^+ decays (delayed ν_e and $\bar{\nu}_\mu$). Thus the neutrino flux consists of a monochromatic neutrino line at $E_\nu = (m_\pi^2 - m_\mu^2)/2m_\pi \simeq 30$ MeV and two continuous spectra.

The spectral functions are given by

$$\begin{aligned} \mathcal{F}_{\nu_\mu}(E_\nu) &= \frac{2m_\pi}{m_\pi^2 - m_\mu^2} \delta\left(1 - \frac{2E_\nu m_\pi}{m_\pi^2 - m_\mu^2}\right), \\ \mathcal{F}_{\nu_e}(E_\nu) &= \frac{192}{m_\mu} \left(\frac{E_\nu}{m_\mu}\right)^2 \left(\frac{1}{2} - \frac{E_\nu}{m_\mu}\right), \\ \mathcal{F}_{\bar{\nu}_\mu}(E_\nu) &= \frac{64}{m_\mu} \left(\frac{E_\nu}{m_\mu}\right)^2 \left(\frac{3}{4} - \frac{E_\nu}{m_\mu}\right). \end{aligned} \quad (15)$$

For a pion-at-rest source $E_\nu^{\max} = m_\mu/2$ where $m_\mu = 105.65$ MeV is the muon mass [29]. The neutrino flux is then obtained by normalizing these spectral functions to $n_{\text{POT}} \times r/4\pi L^2$, where n_{POT} refers to the number of protons at target (1.76×10^{23} over 308.1 live-days of neutrino detection for the COHERENT CsI detector [1]), $r = 0.08$ is the number of neutrinos produced per proton-mercury collision and $L = 20$ m is the detector location from the collision point. To convert the exposure time to a whole year we scale n_{POT} by 365/308.1.

As for reactors, we use the Kopeikin neutrino spectral data points [32] normalized under the assumption of 6 anti-neutrinos and 200 MeV of energy per fission on average. Assuming a generic 1 GW reactor with an isotropic flux at a distance L/cm from the detector we estimate the number of neutrinos to be

$$n_{\text{reactor}}(L) = \frac{1.5 \times 10^{19}}{(L/\text{cm})^2} \text{cm}^{-2} \text{s}^{-1}. \quad (16)$$

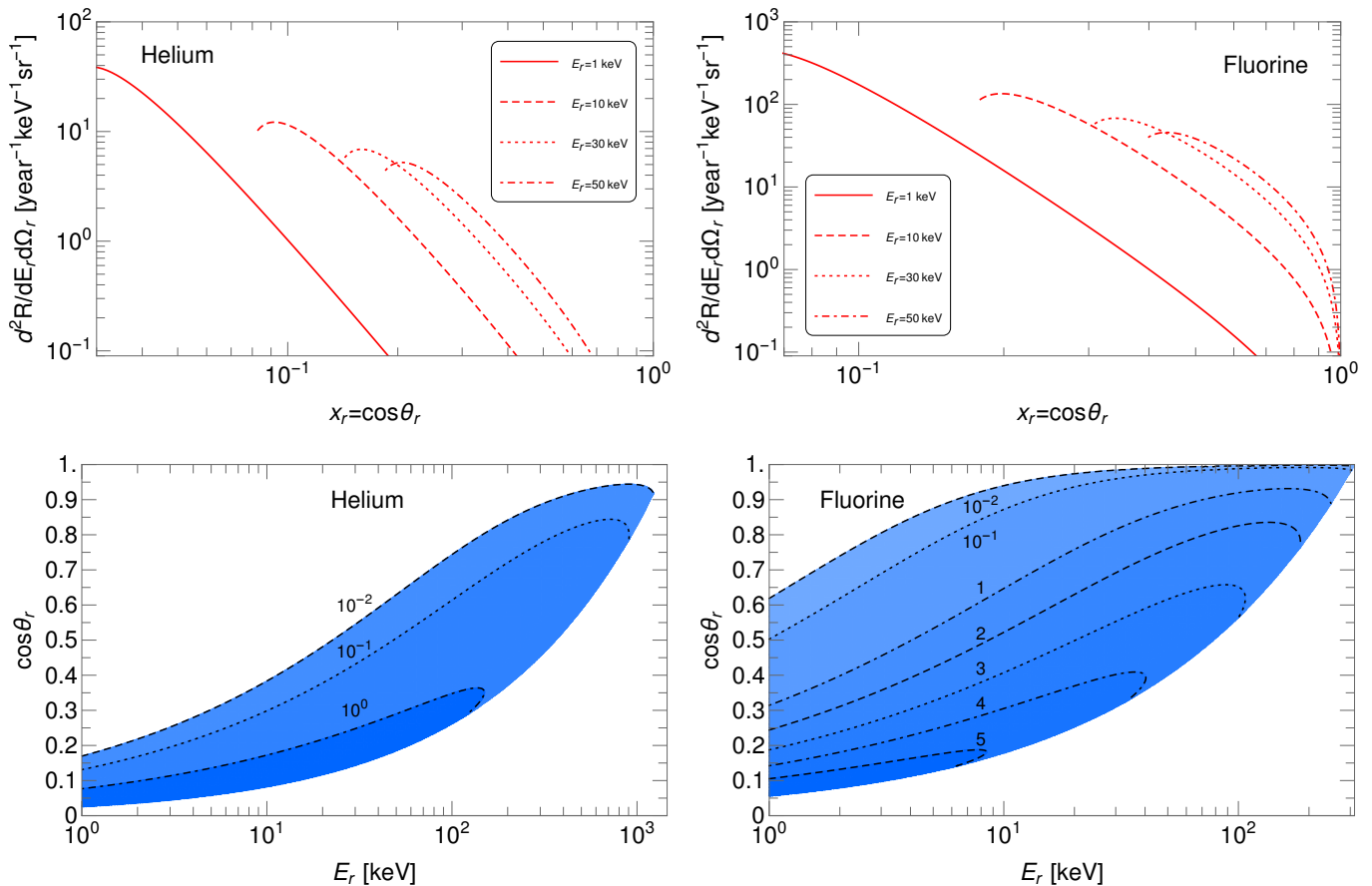


FIG. 2. **Top:** Nuclear recoil energy, E_r , slices of the DRS as a function of $\cos\theta_r$ for He (left) and F (right) detectors. The DRS curves are limited on the left by the maximum neutrino flux energy. **Bottom:** Contours of the same DRS in the $\cos\theta_r$ - E_r plane.

It is important to note that both sources are modeled as point-like. This is not a big issue for energy measurement, but for an angular measurement using the actual size of the source leads to an irreducible uncertainty of roughly the angular size of the source as viewed from the detector. For example, a 1 GW reactor core of 4 m height and 3 m diameter at a distance of 20 m has an angular size of about 10° . We continue with this point-like source approximation, and discuss below the impact of this assumption.

B. Detectors

We will restrict ourselves to helium (He) and fluorine (F) detectors which, given their natural isotopes abundances, are mainly composed of ^4He and ^{19}F . We consider F because it is a standard gas used for directional dark matter detection, and consider He because it gives us an example of a very light nuclear target. For concreteness we will assume a useable (fiducial) detector mass of 1 tonne located 20 m away from the source. A 1000 m^3 detector at normal temperature and pressure amounts to about 164 kg of He and 1555 kg of F. In reality, however, in a drift chamber with directional sensitivity the target gas is at a partial pressure of about 1/75 and

somewhere between 10% and 40% of the mass is not useable².

We assume the detectors to have 100% efficiency, perfect energy and angular resolution, and do not model any backgrounds since we are interested purely in the signal. In reality, the efficiency is expected to deteriorate at small E_r and the angular resolution can vary from 10° to 60° and is often at the expense of energy resolution. We also assume the detectors to be point-like or, equivalently, to have perfect resolution of the location of the scattering event. Unless explicitly stated otherwise, we assume a minimum energy detection threshold of 1 keV.

IV. KINEMATICS

We now move on to discuss kinematic limits applicable to our analysis. The recoil energy can be expressed either in terms of the scattering angle of the neutrino, $\cos\theta$, or the nu-

² Private communication with Neil Spooner and Sven Vahsen

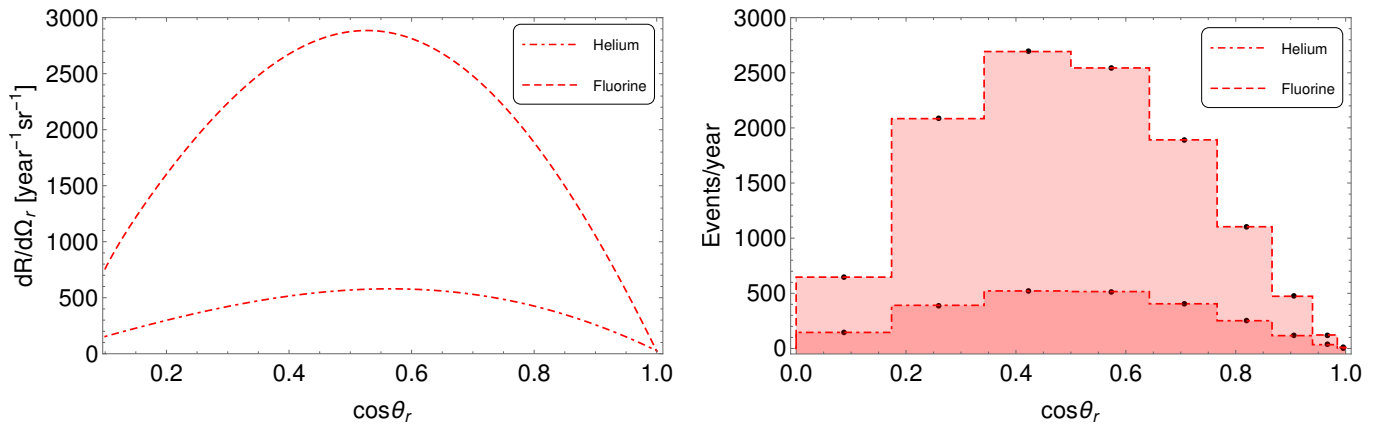


FIG. 3. **Left:** The angular spectra of SNS neutrinos for He and F detectors in the SM. The peaks occur at $\cos \theta_r \simeq 0.56$ for He and $\cos \theta_r \simeq 0.51$ for F, which translates into $\theta_r \simeq 56^\circ$ and $\theta_r \simeq 59^\circ$ respectively. **Right:** The event yield per year in angular bins of size of $|\Delta\theta_r| = 10^\circ$. The total yield is roughly 2300 events for He and 11200 for F.

cleus, $\cos \theta_r$. In the laboratory frame they read

$$E_r = \frac{E_\nu^2(1 - \cos \theta)}{m_N + E_\nu(1 + \cos \theta)},$$

$$E_r = \frac{2m_N E_\nu^2 \cos^2 \theta_r}{(E_\nu + m_N)^2 - E_\nu^2 \cos^2 \theta_r}. \quad (17)$$

From these expressions one can see that the maximum recoil energy is obtained at forward neutrino scattering ($\theta = \pi$) and $\theta_r = 0$, while for $\theta = 0$ and $\theta_r = \pi/2$ the recoil energy vanishes. In practice, however, the maximum value for E_r is determined by the kinematics of the ingoing neutrinos, which for the SNS is determined by $E_\nu \leq m_\mu/2$. For our reactor analysis, we set $E_\nu \lesssim E_\nu^{\text{re}} = 9 \text{ MeV}$. This kinematic constraint can be translated into an upper bound on θ_r by using the energy conservation relation $E_\nu = \varepsilon$ with Eq. (13), resulting in

$$\text{SNS: } \cos \theta_r > \frac{1}{m_\mu} \sqrt{\frac{m_N E_r}{2}} \left(2 + \frac{m_\mu}{m_N} \right), \quad (18)$$

$$\text{Reactor: } \cos \theta_r > \frac{1}{E_\nu^{\text{re}}} \sqrt{\frac{m_N E_r}{2}} \left(1 + \frac{E_\nu^{\text{re}}}{m_N} \right).$$

We can see that, for a fixed recoil energy, the heavier the target nucleus the smaller is the maximum recoil angle. For fixed nuclide mass, larger values of recoil energy imply smaller recoil angles. Since (18) is a purely kinematic bound, it is valid regardless of whether or not one assumes new physics contributions.

Another constraint one could place stems from the condition $d^2R/dE_r d\Omega_r \geq 1$, corresponding to the condition of the DRS being measurable. Additionally, in contrast to the kinematic limit discussed above, this limit *does* depend on the presence of new physics. If the new contribution enhances (reduces) the DRS ³ a wider (narrower) $\cos \theta_r$ region can be measured.

³ Sizable reductions are possible only for a vector contribution (destructive

The limits are illustrated in Fig. 1 which shows the possible angular distributions for one-tonne helium (left graph) and fluorine (right graph) directional detectors with SNS neutrinos. Note that we include $\theta_r \rightarrow -\theta_r$ for illustration. The measurable angular region is that within the dotted and solid curves and can be extended further towards zero degrees by increasing the exposure. One can see that He detectors have access to larger angles than F detectors due to the lower mass of the target. The dashed curves correspond to the angular distribution of ν_μ -induced events. It follows from the condition $E_\nu = \varepsilon = (m_\pi^2 - m_\mu^2)/2/m_\pi$ which translated into $\cos \theta_r$ reads

$$\cos \theta_r^{\nu_\mu} = \frac{2m_\pi}{m_\pi^2 - m_\mu^2} \sqrt{\frac{m_N E_r}{2}} \left(1 + \frac{m_\pi^2 - m_\mu^2}{2m_\pi m_N} \right). \quad (19)$$

V. STANDARD MODEL SIGNATURES

A. SNS neutrinos

With the aid of Eq. (14) we can calculate the DRS as a function of nuclear recoil angle for different recoil energy values. Fig. 2 shows slices of fixed E_r of the DRS and contours in the E_r - $\cos \theta_r$ plane for helium and fluorine. Note that we omit the prompt neutrino contributions since they would manifest as a δ -function.

Notice that F leads to markedly higher event rates and allows access to a much larger range of energies and angles due to its mass. One small trade off is that He can lead to larger scattering angles for the same recoil energy. This can be seen by comparing the endpoints of the red curves of the same energy.

interference). Scalar interactions to a certain degree can destructively interfere as well, but the amount of reduction is proportional to either left-right neutrino mixing (in the case of Dirac couplings) or neutrino masses (in the case of Majorana couplings).

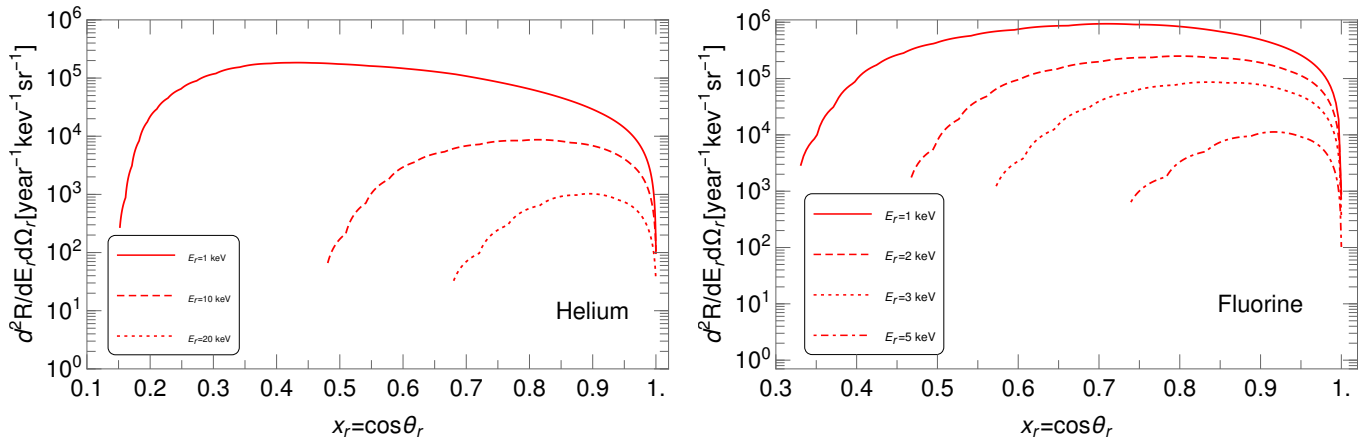


FIG. 4. Nuclear recoil energy, E_r , slices of the DRS as a function of $\cos\theta_r$ at He (left) and F (right) detectors from reactor neutrinos.

Another observation is that low E_r events populate regions of large θ_r and produce substantially more events than high E_r . The contours also show that, for He, a sizable region of the DRS is within $E_r \lesssim 100$ keV and $\cos\theta_r \lesssim 0.3$ whereas F results in a much wider region that spans values up to $E_r \simeq 300$ keV and $\cos\theta_r \simeq 0.9$. This result is expected; smaller incoming neutrino energies induce smaller recoils for which $\cos\theta_r \rightarrow 0$ (see Eq. (17)), and around such energies the neutrino flux is more abundant. As the incoming neutrino energy increases the recoils become more pronounced, thus leading to larger $\cos\theta_r$ and less events due to the lower neutrino flux.

The angular behavior can be more easily understood by examining the angular spectrum, which can be obtained either by integrating the DRS over E_r (Eq. (4)) or by making a change of variable $E_r \rightarrow \cos\theta_r$ in the recoil spectrum (Eq. (1)). The resulting distribution is shown in Fig. 3 both as a continuous curve and a histogram with a bin size of $|\Delta\theta_r| = 10^\circ$. The plots show more clearly the larger event rate in F detectors compared to He detectors, everything else being equal. The SM cross section decreases linearly with E_r (Eq. (3)) while the flux samples central values of E_r . The combination leads to a peak around $\theta_r = 56^\circ$ for He and $\theta_r = 59^\circ$ for F and a rapidly decaying distribution at large $\cos\theta_r$, which are associated with maximum recoil energies. Note that the curves do not extend all the way to $\cos\theta_r = 0$; they are truncated at about $\cos\theta_r = 0.026$ (or 89°) for He and 0.057 (87°) for F due to the assumed 1 keV detector threshold and the maximum neutrino flux energy. The one ton-year exposure yield is about 2300 events for He and 11200 for F.

B. Reactor neutrinos

For nuclear reactors the flux decreases almost monotonically above 1 MeV, which is the smallest accessible energy with a 1 keV detector threshold, and becomes negligible at around 9 MeV. We cut off the flux at around this value leading to a maximum possible E_r of 43 keV for He and 9 keV for F.

The DRS slices are shown in Fig. 4 (note the smaller values

of E_r compared to Fig. 2). The F detector is not able to access small $\cos\theta_r$ as compared with a pion source due to the lower maximum neutrino energy. This is seen more clearly in Fig. 5 (histogram bin size is 30°) where the F distribution decays rather quickly at around $\cos\theta_r = 0.35$. On the flip side, both the He and F curves show a remarkably larger number of total events compared to SNS. Note, however, that a fair comparison of the two sources requires at least accurate modeling of backgrounds and timing information.

VI. NEW PHYSICS SIGNATURES

A. The Models

To examine the capability of directional detectors to identify the presence of new physics, we consider simplified models of light vector or scalar mediators, which have been studied, for example, in Refs. [5, 11, 33–37]. These simplified scenarios can be accommodated in the context of gauge invariant models, e.g., $L_\mu - L_\tau$ [38, 39], $U(1)_{B-L}$ [40–42], $U(1)_{T_{3R}}$ [43, 44], $U(1)'$ [45, 46]. Both scalar and vector mediators can appear concurrently in the context of realistic models. In addition, same type of mediator with different masses and couplings can exist in models. Here we adopt a phenomenological approach in which only couplings relevant for CEvNS are considered.

We will only consider interactions that are lepton flavor universal and conserving. The vector mediator scenario is described by [36, 47]

$$\mathcal{L}_V = \bar{\nu}(f_V + i\gamma_5 f_A)\gamma_\mu \nu V^\mu + \sum_{q=u,d} h_V^q \bar{q}\gamma_\mu q V^\mu + \text{H.c.} \quad (20)$$

One could also introduce a dark charge leading to CP-violating effects as done in Ref. [36]. We do not pursue such features in this study.

For scalar interactions the set of couplings depends on whether or not right-handed neutrinos are present. The La-

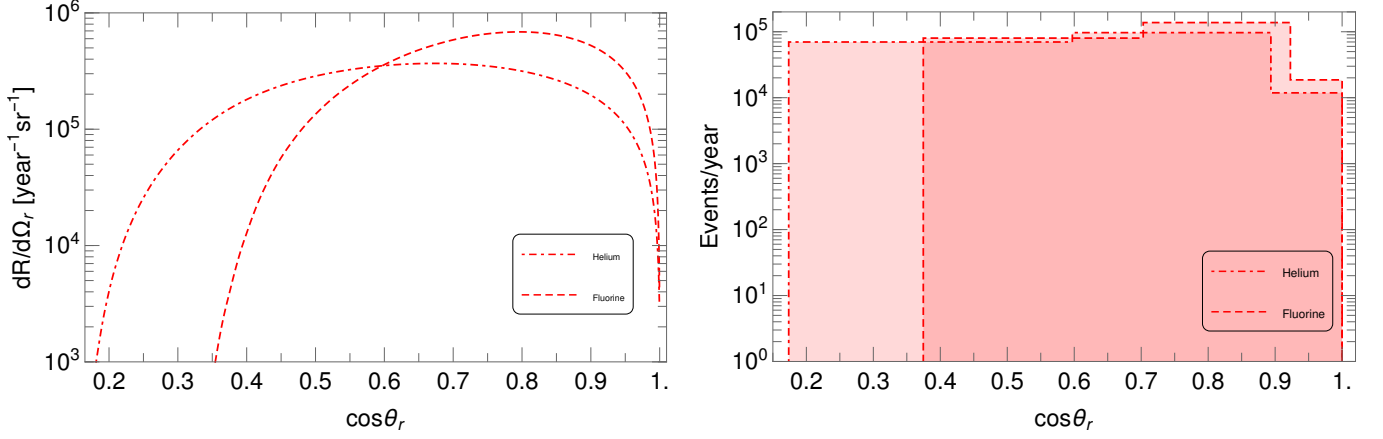


FIG. 5. **Left:** The angular spectra of reactor neutrinos for He and F detectors in the SM. **Right:** The event yield per year in angular bins of size of $|\Delta\theta_r| = 30^\circ$.

grangian we use is given by [11, 36, 47]

$$\mathcal{L}_S = \bar{\nu}(f_S + i\gamma_5 f_S)\nu S + \sum_{q=u,d} h_S^q \bar{q} q S + \text{H.c.} \quad (21)$$

In the lepton number violating case the neutrino coupling has to be recast according to $\nu^T C(f_S + i\gamma_5 f_S)\nu S$. As with the vector mediator, the scalar can be charged under a dark symmetry. We do not consider axial or pseudoscalar quark couplings since their contribution to the CEvNS cross section is small.

The quark-quark operators in Eqs. (20) and (21) induce the following nucleus-nucleus couplings

$$\begin{aligned} \text{Vector: } C_V^N &= Z(2h_V^u + h_V^d) + N(h_V^u + 2h_V^d), \\ \text{Scalar: } C_S^N &= Z \sum_q h_q^S \frac{m_n}{m_q} f_{T_q}^n + N \sum_q h_q^S \frac{m_p}{m_q} f_{T_q}^p, \end{aligned} \quad (22)$$

where $m_{n,p}$ are the neutron and proton masses respectively, q is a quark label, and $f_{T_q}^{n,p}$ refer to hadronic form factors obtained in chiral perturbation theory using measurements of the π -nucleon sigma term [48–50], with the most up-to-date values given by [49]

$$\begin{aligned} f_{T_u}^p &= (20.8 \pm 1.5) \times 10^{-3}, \quad f_{T_d}^p = (41.1 \pm 2.8) \times 10^{-3}, \\ f_{T_u}^n &= (18.9 \pm 1.4) \times 10^{-3}, \quad f_{T_d}^n = (45.1 \pm 2.7) \times 10^{-3}. \end{aligned} \quad (23)$$

For vector interactions the contributions to the CEvNS cross section are obtained from Eq. (3) by the substitution $g_V \rightarrow g_V + \xi_V$ [5, 36], where ξ_V reads

$$\xi_V = \frac{C_V^N F_V}{\sqrt{2} G_F (2m_N E_r + m_V^2)}, \quad (24)$$

with $F_V = f_V - if_A$. The combination $g_V + \xi_V$ leads to constructive or destructive interference depending on the relative sign and size of the SM and NP contribution. Scalar interactions do not interfere with the SM at leading order and their

contribution to the cross section, which has to be added to the SM piece Eq. (3), is written as [11]

$$\frac{d\sigma_S}{dE_r} = \frac{G_F^2}{2\pi} m_N \xi_S^2 \frac{m_N E_r}{2E_r^2}, \quad (25)$$

with the new physics parameters encoded in

$$\xi_S = \frac{C_S^N F_S}{G_F (2m_N E_r + m_S^2)}, \quad (26)$$

where $F_S = f_S - if_P$.

The type of vector and scalar light mediator scenarios described by the interactions in (20) and (21) are subject to a set of constraints, which have been discussed at length, for example, in Refs. [10, 11, 36, 47]. They can be classified into laboratory bounds, and astrophysical and cosmological bounds. In the first category most of the limits apply provided the mediators couple to charged leptons. In our case these couplings are only present at the one-loop order and so can be safely ignored. Other limits apply only on the neutrino-quark (nucleon level) couplings, so they can be readily satisfied without drastically diminishing the CEvNS signals. Bounds in the second category can be tight but are subject to relatively large uncertainties and can be circumvented through additional new physics [51, 52] (an exception are limits from BBN, see discussion in Sec. VI B).

One of the most relevant bounds on the interactions in (20) and (21) comes from COHERENT measurements. A recent study, using a likelihood analysis that combines energy and timing data, places bounds for $m_X = 1.0$ MeV ($X = V, S$) [47]. The bounds are derived using a CsI target and can be rescaled by A_i/A_{Cs} to convert them to the cases of He and F. The resulting bounds are:

$$\text{He: } F_V C_V^N \leq 2.2 \times 10^{-8}, \quad F_S C_S^N \leq 1.5 \times 10^{-8}, \quad (27)$$

$$\text{F: } F_V C_V^N \leq 1.1 \times 10^{-7}, \quad F_S C_S^N \leq 7.3 \times 10^{-8}. \quad (28)$$

These values generate the maximum number of events consistent with available data and will be used for the following analysis.

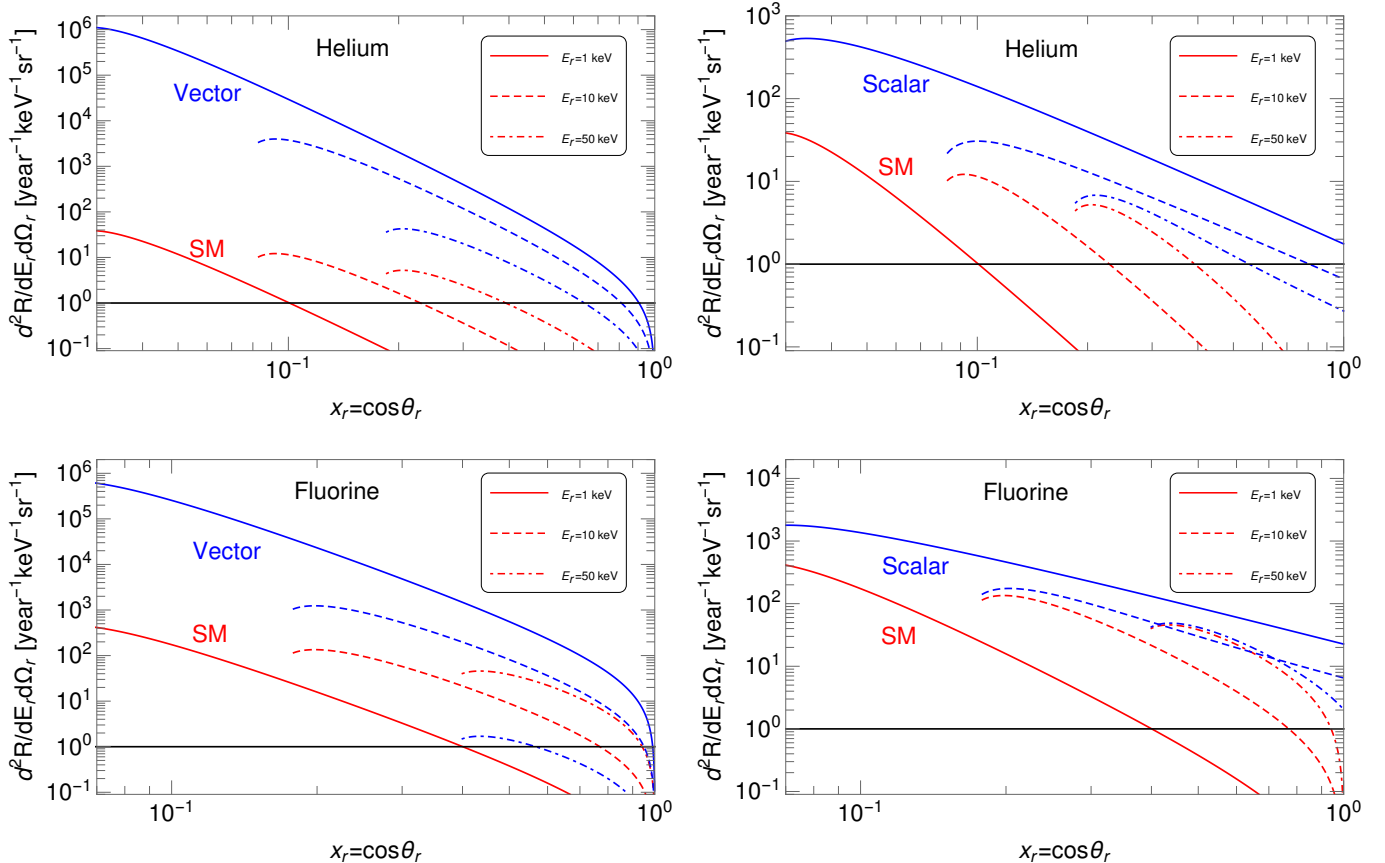


FIG. 6. **Left:** DRS slices of fixed recoil energy as a function of nuclear recoil scattering angle for a vector mediator (blue curve) at a He (Top) and F (bottom) detector using SNS neutrinos. The red curve shows the SM result and the black curve indicates the single event threshold. **Right:** The same plot for the scalar mediator scenario.

B. New physics signals from SNS neutrinos

We can now use Eqs. (3), (14), (24) and (25) combined with $g_V \rightarrow g_V + \xi_V$ to calculate the DRS in the presence of light vector and scalar mediators. The results are displayed in Fig. 6 for both He and F.

For the He case with a vector mediator, all the curves displayed exhibit a large enhancement bringing them above the single event line for most of the $\cos\theta_r$ domain. As we will show there is not always an enhancement, and in the case of F the $E_r = 50$ keV curve with the presence of a vector is far below the SM analogue due to destructive interference. The behavior near $\cos\theta_r = 1$ is mostly unchanged since the SM cross section is also vector mediated. For the scalar case, we can see that the enhancement is larger in the forward direction. However, the enhancement over the SM is significantly smaller than in the vector case even with the He detector.

The angular spectrum is shown in Fig. 7 where the NP features can be seen more transparently. The vector leads to a modest deficit for $\cos\theta_r > 0.5$ while the scalar leads to a small enhancement. For $\cos\theta_r < 0.5$ the rate grows tremendously as we approach $\cos\theta_r = 0$ in the vector scenario. In contrast, the rate remains constant in the scalar scenario but with a sizable

excess over the SM at a He detector.

So far we have discussed the results for 1 MeV mediator masses. However, such species suffer from the tight constraints on the number of effective relativistic degrees of freedom in the early universe. This is encoded in the quantity ΔN_{eff} which is precisely determined through the CMB measurements by the Planck satellite experiment [53]. The constraint has been considered in the context of light mediator models recently [43, 54–57]. The light mediator contribution to ΔN_{eff} can be made negligible while contributing significantly to CEvNS by making the mediator heavy enough (larger than a few MeV) that its abundance is negligible due to Boltzmann suppression at the time of neutrino decoupling. Below, we discuss scenarios with mediator masses > 1 MeV.

To examine how the shape distortion changes with the mediator mass, we plot the angular spectrum as a function of $\cos\theta_r$ for mediators masses 1, 10, 30, and 50 MeV in Fig. 8, for different assumed recoil threshold energies. The discontinuities occur due to prompt neutrinos being unable to induce recoils above a certain angle for a given detection energy threshold (the analogue of Eq. (18) for prompt neutrino energies).

For He, a 30 MeV mediator still modifies the shape of the

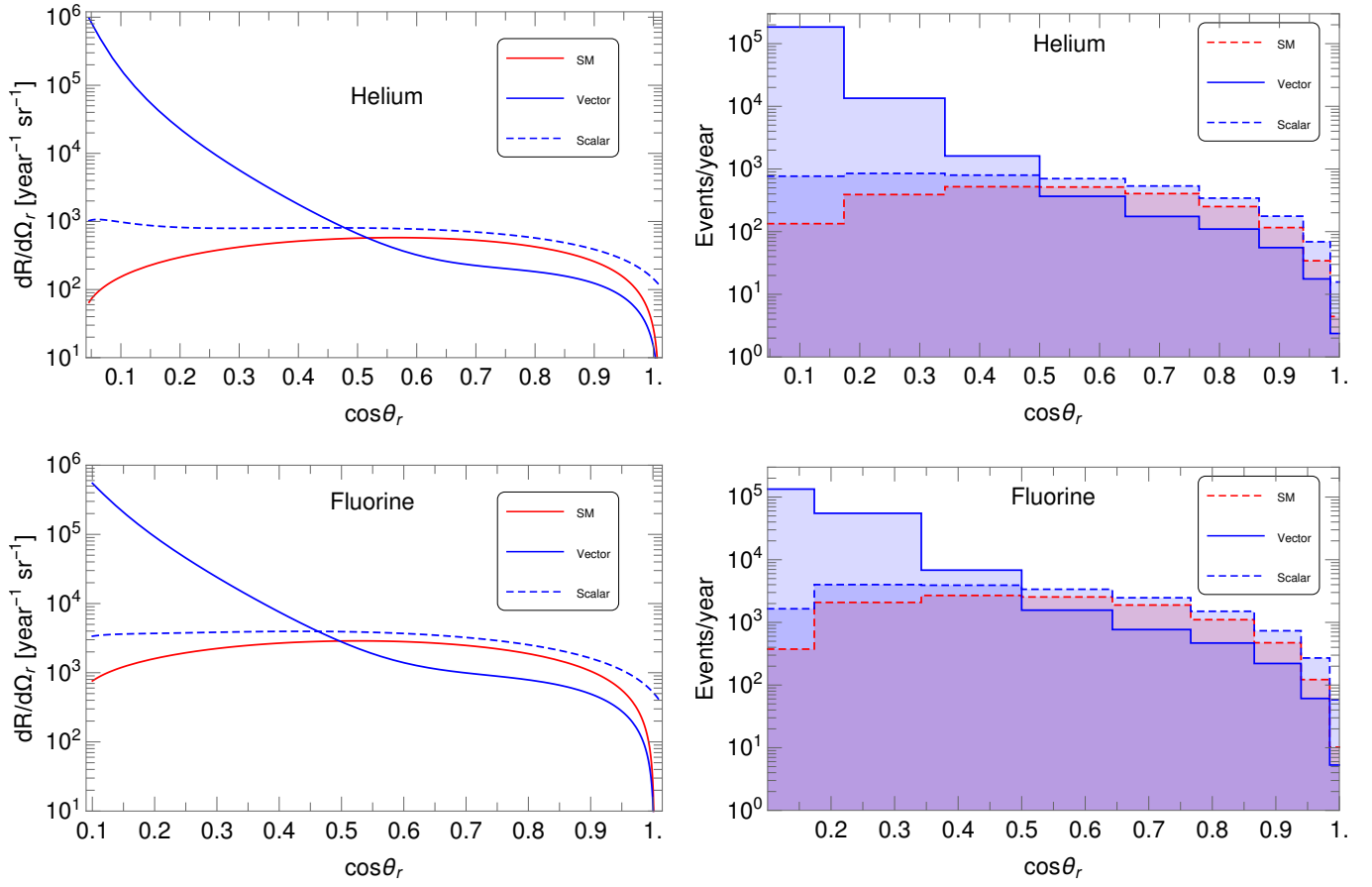


FIG. 7. **Left:** The angular distributions in the SM (solid red), vector (solid blue) and scalar (dashed blue) for He (Top) and F (Bottom) detectors using SNS neutrinos. **Right:** The corresponding event yield in angular bins of size 10° .

distribution although with a deficit instead of an excess, while a 50 MeV mediator only leads to a rescaling of the SM spectrum. For F, at 30 MeV mediator mass the NP spectrum is already a rescaling. As the energy threshold is increased, both the discontinuity and the lower end of the distribution move towards larger $\cos\theta_r$.

Since detectors sensitive to E_r already exist and angular information could come at an expense of energy resolution, it is useful to compare the angular spectrum with the associated energy spectrum (Fig. 9). The vector induced deficit is more dramatic than in the angular distribution and occurs at large values of E_r , which are accessible with current technology. The scalar curve at high recoil energies coincides with that of the SM. Finally, one can note that dips in the recoil spectra are smeared out in nuclear angle space. For example, in helium and for $m_V = 30$ MeV the recoil spectra exhibits a well localized dip at about $E_r = 70$ keV. At the angular distribution level, that sharp downward spike results in a way less pronounced feature at $\cos\theta_r \simeq 0.3$.

It is insightful to use Fig. 9 in conjunction with Fig. 8 to understand the effect of detector thresholds on observables. From Fig. 9 one can directly read off the recoil spectrum from any energy threshold between 1 keV and 100 keV, and a higher

value necessarily leads to lower NP sensitivity. This can be compared to one of the representative threshold values in Fig. 8 to see how the shape discrimination appears in the angle domain.

The excess regions are more interesting to compare since with larger signals backgrounds and systematic errors become less challenging. Comparing the plots we can see a qualitatively unique feature in the lower $\cos\theta_r$ distribution compared to that of low E_r : the three scenarios (SM, SM+Vector, and SM+Scalar) lead to slopes that are negative, positive and vanishing respectively. The discriminating region in the energy domain is roughly between 1 keV and 100 keV, while in the angle domain it is between 85° and 60° . It is unclear at this stage which choice would lead to stronger limits. For that a likelihood analysis using various combinations of detector resolutions is necessary.

One crucial difference is that increasing the detection threshold, say, to 10 keV would eliminate a large portion of the signal discrimination region, while the small $\cos\theta_r$ region would still be accessible. In other words, it could be beneficial to trade a higher detection threshold with finer angular resolution at large angles. The ratios of events with NP to that in the

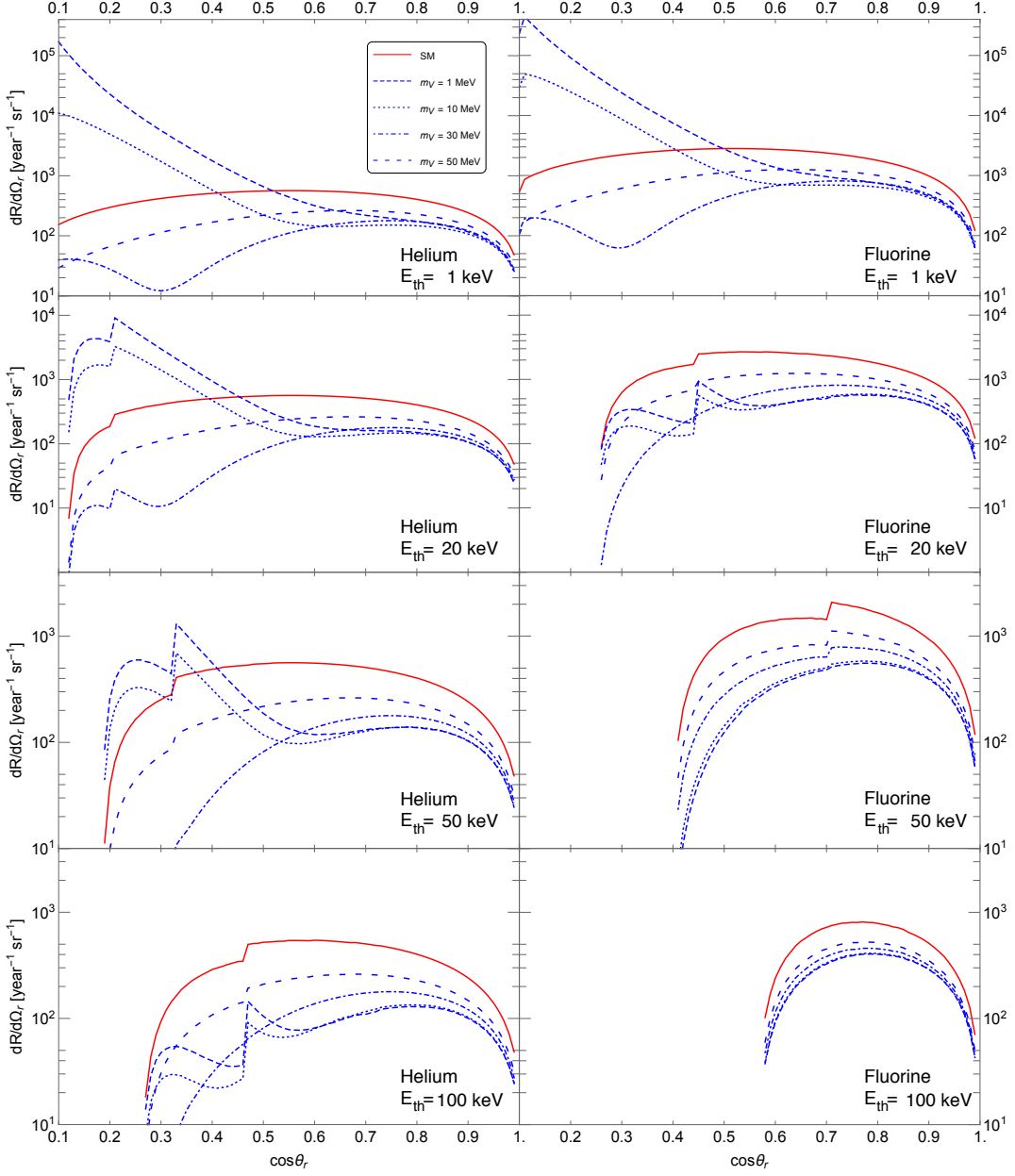


FIG. 8. Angular spectrum as a function of $\cos\theta_r$ in He (left) and F (right) detectors for the SM (red) and with 1, 10, 30, and 50 MeV vector mediator masses. The nuclear recoil energy threshold for each panel is indicated.

SM are

$$\text{He: } N_V/N_{\text{SM}} = 106, \quad N_S/N_{\text{SM}} = 1.8, \quad (29)$$

$$\text{F: } N_V/N_{\text{SM}} = 23, \quad N_S/N_{\text{SM}} = 1.6. \quad (30)$$

C. New physics signals from reactor neutrinos

Finally, we turn to new physics signals at reactors. The event rate is enormous, though as is seen in the DRS slices in Fig. 10, most of the events have very low E_r , particularly

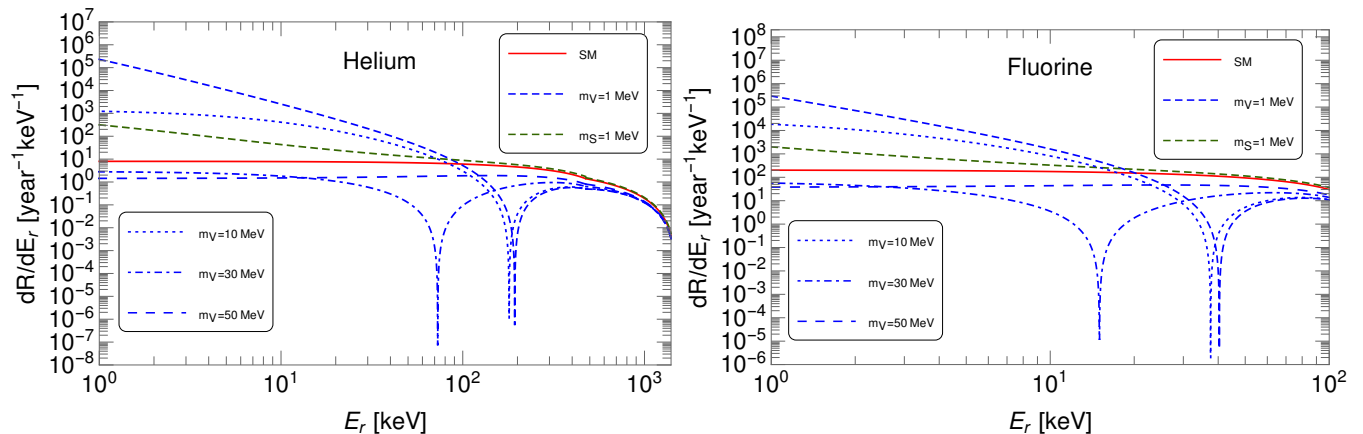


FIG. 9. The recoil energy spectrum in the SM (solid red), vector (solid blue) and scalar (dashed blue) for He (Left) and F (Right) detectors using SNS neutrinos. Included are recoil spectra for different vector boson masses.

in the F case. Examining the angular distribution in Fig. 11, we see that the distribution in the vector scenario is similar to that of the SM and differs only by a scaling factor. This is due in part to the vector nature of the SM interaction and in part due to energy scale of the recoil being much smaller than the mass of the mediator (1 MeV). With an SNS like source, the differences in shapes persist even with 10 MeV mediators but cease at values closer to 100 MeV.

In contrast, the scalar mediator leads to a qualitatively different spectral shape which could potentially be resolved with enough data, and unlike in the SNS source, the excess over the SM is substantial.

VII. CONCLUSIONS

We have performed a theoretical study of the directional behavior of CEvNS using stopped-pion and reactor sources. We consider gaseous helium and fluorine detectors, and generate predictions for the SM nuclear recoil distributions. In addition, we consider scenarios with the addition of light vector or scalar mediators. These light mediators can arise in the context of anomaly free $U(1)_{B-L}$, $U(1)_{T_{3R}}$, $U(1)_{L_{\mu}-L_{\tau}}$ symmetry models. In the context of new symmetry models, we can have multiple copies of same type of mediators and/or different types of mediators being present. The direction information would provide an important additional handle to investigate all these new models. We have identified angular features that can aid in identifying vector mediators at a stopped-pion source such as SNS, and for scalar mediators at reactors. We also provided information on the interplay between energy sensitivity and threshold, and directional sensitivity.

Though our analysis has focused on CEvNS and how new physics may be extracted through neutrino interactions, it would also be interesting to extend our analysis to understand the importance of directionality in low mass dark matter searches using both stopped-pion and reactor sources.

Stopped-pion based experiments like COHERENT have been shown to be valuable probes of sub-GeV dark matter [58], especially since timing and recoil energy information is able to effectively reduce SM and experimental backgrounds [22, 58]. Extending beyond nuclear recoils, it is also interesting to considering directionality in electron recoils. This may even provide new means to discriminate backgrounds and identify new signals via Migdal electrons [59]. Even for energy-only based analyses, including the Migdal effect has been shown to improve bounds on low-mass dark matter in xenon detectors [60].

An obvious next step is to perform a more thorough, likelihood based analysis using more realistic modeling of the experimental setup. For example, this includes modeling the source as an extended object which leads to angular uncertainty. Another example is accounting for backgrounds which limit the significance of the signal. Using realistic fiducial detector masses, which would likely be smaller than the values used here, is necessary for accurate estimates of exposure. More importantly, factoring in the prospective efficiency curves as well as the spatial, energy, and angular resolutions could dramatically alter all the spectral shapes in this study and reframe the interplay between energy and directional information. Directionality in CEvNS is a new and unexplored territory with new ideas, questions and answers to be tapped by the neutrino community.

ACKNOWLEDGEMENTS

We thank Neil Spooner, Sven Vahsen, Kate Scholberg, and Phil Barbeau discussions on this paper. DAS is supported by the grant “Unraveling new physics in the high-intensity and high-energy frontiers”, Fondecyt No 1171136. BD and LES acknowledge support from DOE Grant de-sc0010813. We thank the organizers of the “Magnificent CEvNS 2019 Workshop” where this work was initiated.

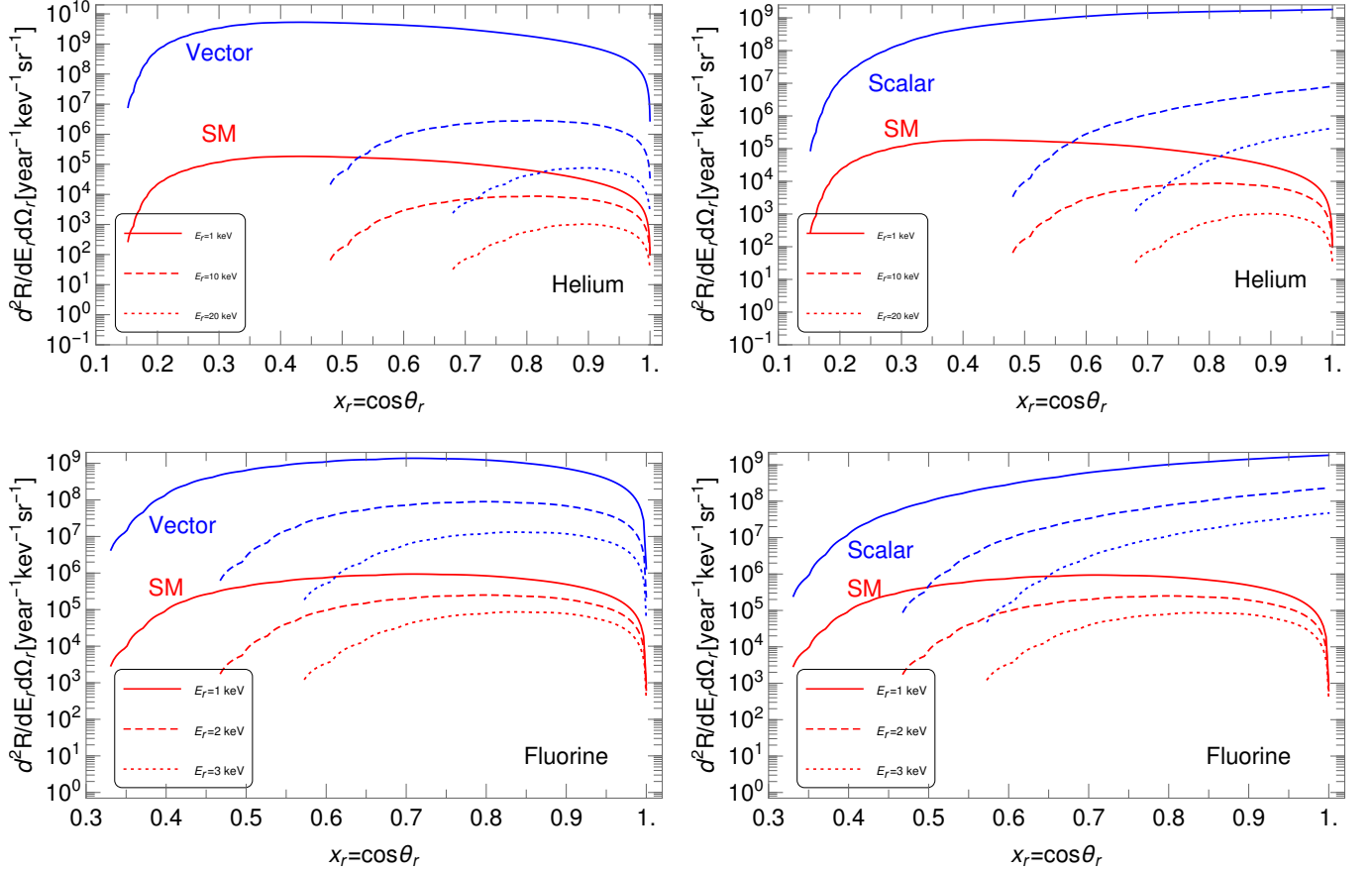


FIG. 10. **Left:** DRS slices of fixed recoil energy as a function of nuclear recoil scattering angle for a vector mediator (blue curve) at an He (Top) and F (bottom) detector using reactor neutrinos. The red curve shows the SM result. **Right:** The same plot for the scalar mediator scenario.

-
- [1] D. Akimov et al. (COHERENT), *Science* (2017), 1708.01294.
[2] D. Akimov et al. (COHERENT) (2020), 2003.10630.
[3] P. Coloma, P. B. Denton, M. C. Gonzalez-Garcia, M. Maltoni, and T. Schwetz, *JHEP* **04**, 116 (2017), 1701.04828.
[4] P. Coloma, M. C. Gonzalez-Garcia, M. Maltoni, and T. Schwetz (2017), 1708.02899.
[5] J. Liao and D. Marfatia, *Phys. Lett.* **B775**, 54 (2017), 1708.04255.
[6] J. B. Dent, B. Dutta, S. Liao, J. L. Newstead, L. E. Strigari, and J. W. Walker, *Phys. Rev.* **D97**, 035009 (2018), 1711.03521.
[7] D. K. Papoulias and T. S. Kosmas, *Phys. Rev.* **D97**, 033003 (2018), 1711.09773.
[8] J. Billard, J. Johnston, and B. J. Kavanagh (2018), 1805.01798.
[9] M. Lindner, W. Rodejohann, and X.-J. Xu, *JHEP* **03**, 097 (2017), 1612.04150.
[10] M. Abdullah, J. B. Dent, B. Dutta, G. L. Kane, S. Liao, and L. E. Strigari, *Phys. Rev.* **D98**, 015005 (2018), 1803.01224.
[11] Y. Farzan, M. Lindner, W. Rodejohann, and X.-J. Xu, *JHEP* **05**, 066 (2018), 1802.05171.
[12] V. Brdar, W. Rodejohann, and X.-J. Xu, *JHEP* **12**, 024 (2018), 1810.03626.
[13] D. Aristizabal Sierra, V. De Romeri, and N. Rojas, *Phys. Rev.* **D98**, 075018 (2018), 1806.07424.
[14] A. Datta, B. Dutta, S. Liao, D. Marfatia, and L. E. Strigari, *JHEP* **01**, 091 (2019), 1808.02611.
[15] E. Ciuffoli, J. Evslin, Q. Fu, and J. Tang, *Phys. Rev.* **D97**, 113003 (2018), 1801.02166.
[16] D. Aristizabal Sierra, J. Liao, and D. Marfatia, *JHEP* **06**, 141 (2019), 1902.07398.
[17] D. K. Papoulias, T. S. Kosmas, R. Sahu, V. K. B. Kota, and M. Hota, *Phys. Lett.* **B800**, 135133 (2020), 1903.03722.
[18] T. S. Kosmas, D. K. Papoulias, M. Tortola, and J. W. F. Valle, *Phys. Rev.* **D96**, 063013 (2017), 1703.00054.
[19] C. Blanco, D. Hooper, and P. Machado (2019), 1901.08094.
[20] B. Dutta, S. Liao, S. Sinha, and L. E. Strigari, *Phys. Rev. Lett.* **123**, 061801 (2019), 1903.10666.
[21] C. Giunti, *Phys. Rev.* **D101**, 035039 (2020), 1909.00466.
[22] B. Dutta, D. Kim, S. Liao, J.-C. Park, S. Shin, and L. E. Strigari (2019), 1906.10745.
[23] F. Mayet et al., *Phys. Rept.* **627**, 1 (2016), 1602.03781.
[24] J. B. R. Battat et al., *Phys. Rept.* **662**, 1 (2016), 1610.02396.
[25] J. D. Lewin and P. F. Smith, *Astropart. Phys.* **6**, 87 (1996).

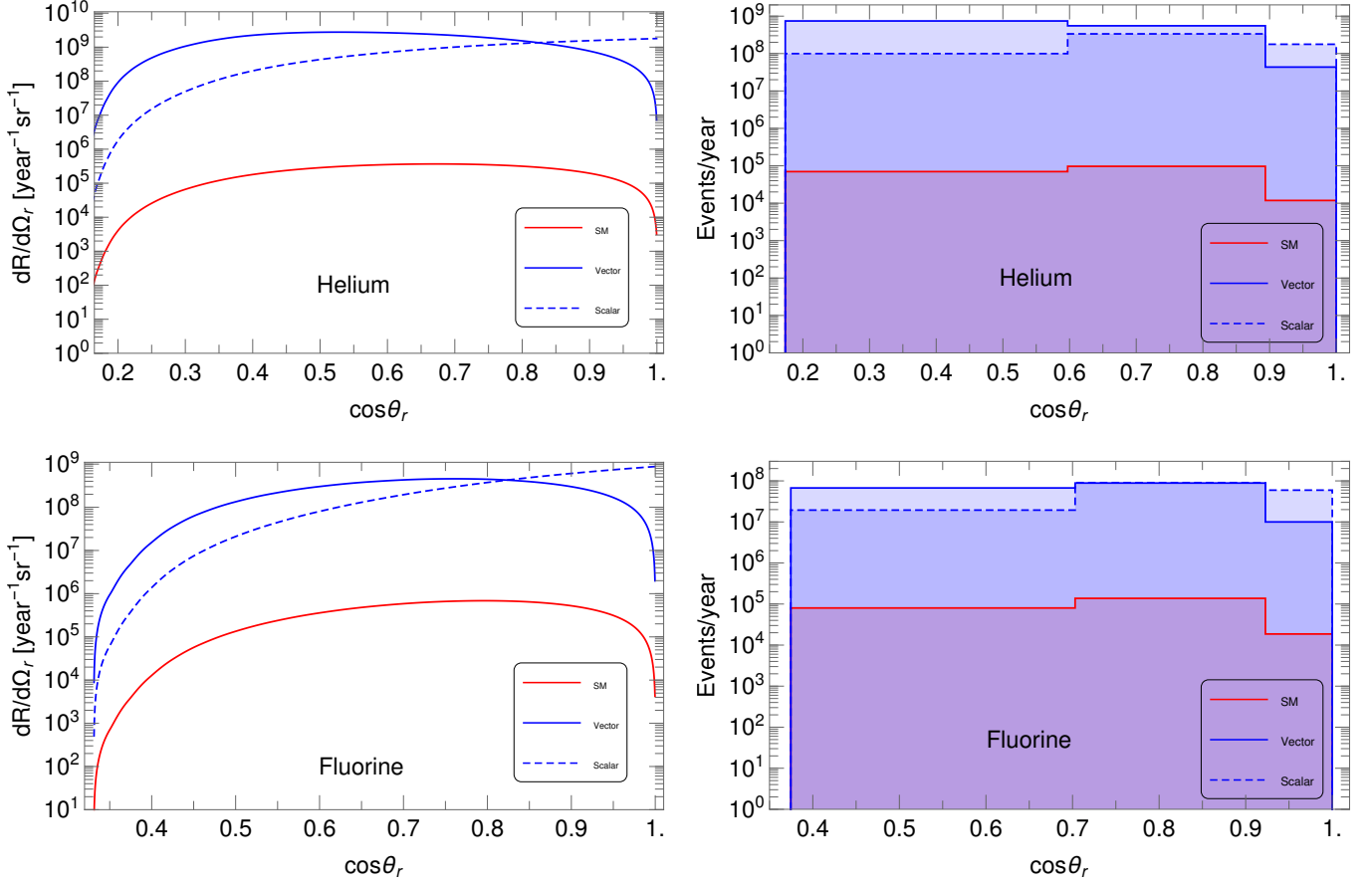


FIG. 11. **Left:** The angular distributions in the SM (solid red), vector (solid blue) and scalar (dashed blue) for He (Top) and F (Bottom) detectors using reactor neutrinos. **Right:** The corresponding event yield in angular bins of size 30° .

- [26] I. Angeli and K. P. Marinova, *Atom. Data Nucl. Data Tabl.* **99**, 69 (2013).
- [27] D. Z. Freedman, *Phys. Rev.* **D9**, 1389 (1974).
- [28] D. Z. Freedman, D. N. Schramm, and D. L. Tubbs, *Ann. Rev. Nucl. Part. Sci.* **27**, 167 (1977).
- [29] C. Patrignani et al. (Particle Data Group), *Chin. Phys.* **C40**, 100001 (2016).
- [30] P. Gondolo, *Phys. Rev.* **D66**, 103513 (2002), hep-ph/0209110.
- [31] C. A. J. O'Hare, A. M. Green, J. Billard, E. Figueroa-Feliciano, and L. E. Strigari, *Phys. Rev.* **D92**, 063518 (2015), 1505.08061.
- [32] V. I. Kopeikin, *Phys. Atom. Nucl.* **75**, 143 (2012), [*Yad. Fiz.*75N2,165(2012)].
- [33] I. M. Shoemaker, *Phys. Rev.* **D95**, 115028 (2017), 1703.05774.
- [34] B. Dutta, S. Liao, L. E. Strigari, and J. W. Walker, *Phys. Lett.* **B773**, 242 (2017), 1705.00661.
- [35] D. Aristizabal Sierra, N. Rojas, and M. H. G. Tytgat, *JHEP* **03**, 197 (2018), 1712.09667.
- [36] D. Aristizabal Sierra, V. De Romeri, and N. Rojas, *JHEP* **09**, 069 (2019), 1906.01156.
- [37] O. G. Miranda, D. K. Papoulias, M. Tórtola, and J. W. F. Valle (2020), 2002.01482.
- [38] X. G. He, G. C. Joshi, H. Lew, and R. R. Volkas, *Phys. Rev.* **D43**, 22 (1991).
- [39] X.-G. He, G. C. Joshi, H. Lew, and R. R. Volkas, *Phys. Rev.* **D44**, 2118 (1991).
- [40] J. Heck, *Phys. Lett.* **B739**, 256 (2014), 1408.6845.
- [41] Y. S. Jeong, C. S. Kim, and H.-S. Lee, *Int. J. Mod. Phys.* **A31**, 1650059 (2016), 1512.03179.
- [42] K. S. Babu, A. Friedland, P. A. N. Machado, and I. Mocioiu (2017), 1705.01822.
- [43] B. Dutta, S. Ghosh, and J. Kumar (2020), 2002.01137.
- [44] B. Dutta, S. Ghosh, and J. Kumar, *Phys. Rev.* **D100**, 075028 (2019), 1905.02692.
- [45] Y. Farzan, *Phys. Lett.* **B748**, 311 (2015), 1505.06906.
- [46] Y. Farzan and I. M. Shoemaker, *JHEP* **07**, 033 (2016), 1512.09147.
- [47] D. Aristizabal Sierra, B. Dutta, S. Liao, and L. E. Strigari, *JHEP* **12**, 124 (2019), 1910.12437.
- [48] A. Crivellin, M. Hoferichter, and M. Procura, *Phys. Rev.* **D89**, 054021 (2014), 1312.4951.
- [49] M. Hoferichter, J. Ruiz de Elvira, B. Kubis, and U.-G. Meiner, *Phys. Rev. Lett.* **115**, 092301 (2015), 1506.04142.
- [50] J. R. Ellis, A. Ferstl, and K. A. Olive, *Phys. Lett.* **B481**, 304 (2000), hep-ph/0001005.
- [51] A. E. Nelson and J. Walsh, *Phys. Rev.* **D77**, 033001 (2008), 0711.1363.
- [52] A. E. Nelson and J. Walsh, *Phys. Rev.* **D77**, 095006 (2008), 0802.0762.
- [53] N. Aghanim et al. (Planck) (2018), 1807.06209.
- [54] A. Kamada and H.-B. Yu, *Phys. Rev.* **D92**, 113004 (2015), 1504.00711.

- [55] S. Knapen, T. Lin, and K. M. Zurek, *Phys. Rev.* **D96**, 115021 (2017), 1709.07882.
- [56] M. Escudero, D. Hooper, G. Krnjaic, and M. Pierre, *JHEP* **03**, 071 (2019), 1901.02010.
- [57] N. Sabti, J. Alvey, M. Escudero, M. Fairbairn, and D. Blas, *JCAP* **2001**, 004 (2020), 1910.01649.
- [58] D. Akimov et al. (COHERENT) (2019), 1911.06422.
- [59] M. Ibe, W. Nakano, Y. Shoji, and K. Suzuki, *JHEP* **03**, 194 (2018), 1707.07258.
- [60] E. Aprile et al. (XENON), *Phys. Rev. Lett.* **123**, 241803 (2019), 1907.12771.